

BATTERIES

Topological defect dynamics in operando battery nanoparticles

A. Ulvestad,¹ A. Singer,¹ J. N. Clark,^{2,3} H. M. Cho,⁴ J. W. Kim,¹ R. Harder,⁵ J. Maser,⁵ Y. S. Meng,^{4*} O. G. Shpyrko^{1*}

Topological defects can markedly alter nanomaterial properties. This presents opportunities for “defect engineering,” where desired functionalities are generated through defect manipulation. However, imaging defects in working devices with nanoscale resolution remains elusive. We report three-dimensional imaging of dislocation dynamics in individual battery cathode nanoparticles under operando conditions using Bragg coherent diffractive imaging. Dislocations are static at room temperature and mobile during charge transport. During the structural phase transformation, the lithium-rich phase nucleates near the dislocation and spreads inhomogeneously. The dislocation field is a local probe of elastic properties, and we find that a region of the material exhibits a negative Poisson’s ratio at high voltage. Operando dislocation imaging thus opens a powerful avenue for facilitating improvement and rational design of nanostructured materials.

Nanoconfinement causes material properties to differ substantially from their bulk counterparts in many ways and can lead to size-tunable thermodynamics, faster intercalation kinetics, and extended life cycles (1). “Defect engineering” can be used to further design and optimize properties owing to the appreciable influence of defects on material properties (2, 3). Motivated by this opportunity, many researchers worked to develop imaging techniques capable of resolving defects, in particular dislocations (4, 5).

The observation of dislocations with techniques such as x-ray topography (6, 7) and reciprocal space mapping dates back to the 1950s (8–10). The coherence of third-generation synchrotron x-ray beams enabled several new defect imaging techniques (11), including phase contrast tomography (12) and Bragg x-ray ptychography (13), which was recently used to visualize the displacement field of a dislocation in silicon. For a recent review of defect imaging using coherent methods, see (14).

Bragg coherent diffraction imaging (BCDI) relies on interference produced by coherent x-rays and phase-retrieval algorithms to reconstruct the three-dimensional (3D) electron density and atomic displacement fields in nanocrystals (15–18). The displacement field information that BCDI provides is complementary to the aforementioned techniques and crucial in identifying the character of single dislocations. BCDI

can also track, with nanoscale resolution, buried single defects under operando conditions.

The role of dislocations in Li-ion battery performance remains largely underexplored, and one of the few areas where materials can be further optimized. The appearance of dislocations correlates with capacity loss (19), as dislocations induce stress and strain (20). Yet, dislocations can relieve strain during phase transformations by allowing the interface between the phases to decohere and thus prevent cracking and the associated active material loss and undesirable surface reactions with the electrolyte (21, 22). To understand these nuances, we must first track single defects in operating devices under working conditions. We use BCDI to study single defects in the nanostructured disordered spinel material $\text{LiNi}_{0.5}\text{Mn}_{1.5}\text{O}_4$ (LNMO). LNMO is a promising high-voltage cathode material in which the lithium diffusion path-

way is three-dimensional (23). In addition, the material exhibits both two-phase coexistence and phase transformations at certain lithium concentrations during charge and discharge, as evidenced by both electrochemical and diffraction data (21, 24–26). The phases are different in their lattice constant but have the same symmetry group ($Fd\bar{3}m$).

The experimental setup is shown schematically in Fig. 1. Focused coherent x-rays are incident on an in situ coin cell (fig. S1) that contains the nanoparticulate LNMO cathode material. X-ray diffraction data (fig. S2) and electrochemical data (fig. S3) confirm expected behavior of the LNMO cathode. The x-rays scattered by a single LNMO particle satisfying the (111) Bragg condition are recorded on an area detector (27). The experimental geometry, combined with the random orientation of the cathode nanoparticles, ensures that the (111) Bragg reflections corresponding to separate particles are well separated and an individual reflection can be isolated on the detector. The battery was cycled 101 times at a fast rate (30 min for full charge) before the imaging experiment. From the coherent diffraction data, we reconstruct both the 3D distribution of electron density, $\rho(x, y, z)$, and the 3D displacement field along [111], $u_{111}(x, y, z)$, in an individual cathode nanoparticle with 35-nm spatial resolution (fig. S4) (27).

Figure 2A shows the isosurface rendering of the particle shape. Figure 2B shows a cross-section of the 3D displacement field [$u_{111}(x, y, z = z_0)$] in the cathode nanoparticle. The [111] direction is approximately along the x axis, whereas the x-ray beam is almost parallel to the z axis. To determine the defect type responsible for the displacement field in Fig. 2, B and C, Fig. 2D shows the displacement field magnitudes at a fixed radius, r , as a function of azimuthal angle, θ . Depending on the defect type, this angular distribution will have distinct features. For example, displacement fields generated by screw dislocations must vary linearly with θ (28). Edge dislocations produce

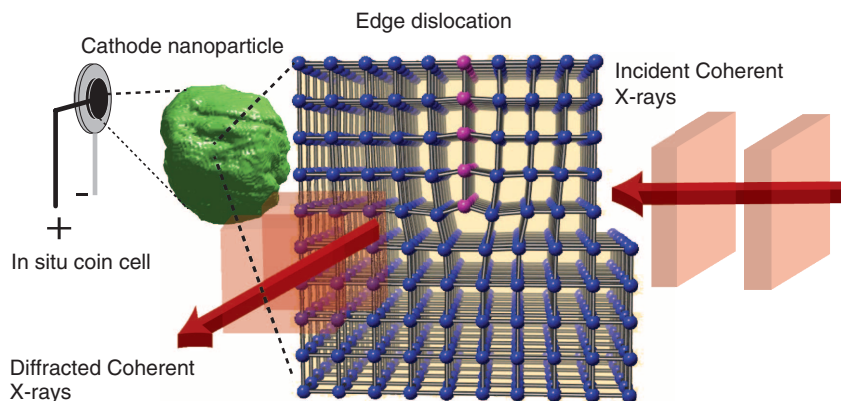


Fig. 1. Bragg coherent diffractive imaging experiment schematic. Coherent x-rays (red) are incident on a cathode nanoparticle (green) containing an edge dislocation. A schematic of an edge dislocation for a cubic unit cell structure is shown with the extra half plane colored purple. The diffracted x-rays carry information about the 3D electron density and atomic displacement fields within the particle that allows the type of dislocation to be identified.

¹Department of Physics, University of California–San Diego, La Jolla, CA 92093-0319, USA. ²Stanford PULSE Institute, SLAC National Accelerator Laboratory Menlo Park, CA 94025, USA. ³Center for Free-Electron Laser Science (CFEL), Deutsches Elektronensynchrotron (DESY), Notkestrasse 85, 22607 Hamburg, Germany. ⁴Department of NanoEngineering, University of California–San Diego, La Jolla, CA 92093-0448, USA. ⁵Advanced Photon Source, Argonne National Laboratory, Argonne, IL 60439, USA.

*Corresponding author. E-mail: shmeng@ucsd.edu (Y.S.M.); oshpyrko@physics.ucsd.edu (O.G.S.)

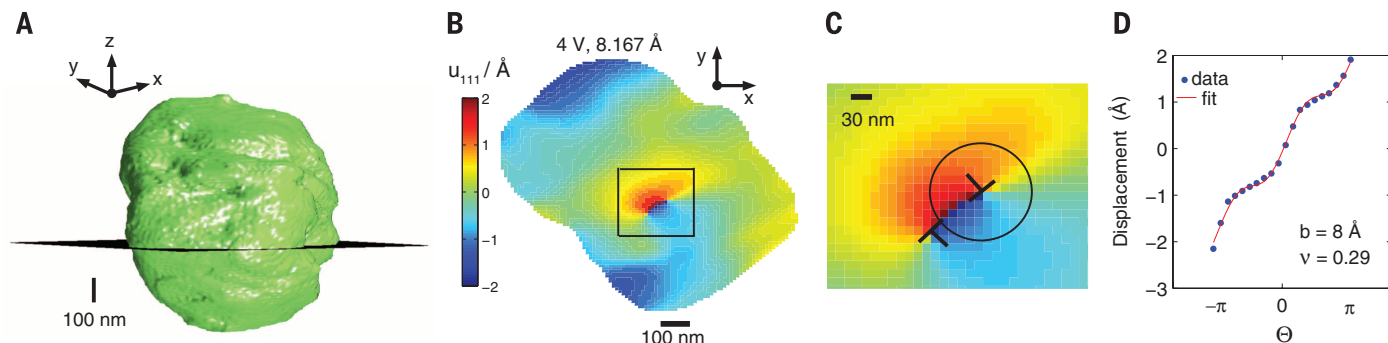


Fig. 2. Edge dislocation displacement field identified in a single LNMO cathode nanoparticle. (A) A green isosurface representing the particle shape. A black plane shows the spatial location of the cross-section of the u_{111} displacement field shown in (B). (C) Magnification of the boxed region in (B). Locations of edge dislocations are indicated by \perp . Data points in (D) correspond to the displacement values as a function of azimuthal coordinate θ at fixed radius r [shown as a black circle in (C)]. The red line is a two-parameter fit to the edge dislocation model described by Eqs. 1a and 1b.

displacements both perpendicular and parallel to the extra half plane given by (28)

$$u_{\perp} = \frac{b}{2\pi} \left(\theta + \frac{\sin 2\theta}{4(1-\nu)} \right) \quad (1a)$$

$$u_{\parallel} = -\frac{b}{2\pi} \left(\frac{1-2\nu}{4(1-\nu)} \log r^2 + \frac{\cos 2\theta}{4(1-\nu)} \right) \quad (1b)$$

where r and θ are the radial and azimuthal coordinate, b is the Burgers vector length, and ν is Poisson's ratio (see fig. S5 for coordinate definition). Thus, an edge dislocation produces a displacement field that varies linearly with θ with an additional periodic modulation. By inspection of Fig. 2D, we identify the displacement field in Fig. 2, B and C, as resulting from edge dislocations.

We quantitatively determined the edge dislocation properties and the elastic properties in the nearby region by using Eqs. 1a and 1b with b and ν as fit parameters (27). Other elastic parameters determined from the displacement field are consistent with expectations (27). The crystallographic geometry of the edge dislocation with respect to $[111]$ is determined from the 3D displacement field to be $50 \pm 8^\circ$, in good agreement with the predicted value of 54° for an edge dislocation along $\langle 100 \rangle$. The fitted Burgers vector magnitude of $8 \pm 1 \text{ \AA}$ is in excellent agreement with the lattice constant along $\langle 100 \rangle$, which is 8.16 \AA , and the fitted Poisson's ratio of 0.27 ± 0.1 agrees with the bulk value of 0.3 in the discharged state (29). For additional fit information, see figs. S6 and S7.

We mapped the edge dislocations in 3D, and by repeated measurements confirmed that they were static for at least an hour at room temperature (fig. S8). Figure 3 shows the evolution of the dislocation line as a function of charging. The width of the dislocation line reflects the uncertainty in the position as determined by the phase retrieval transfer function (27). The evolution of the single-particle lattice constant during charging and discharging is shown in fig. S9.

We observe dislocation line movement as a function of charge transport, which means that the dislocations are stable at room temperature

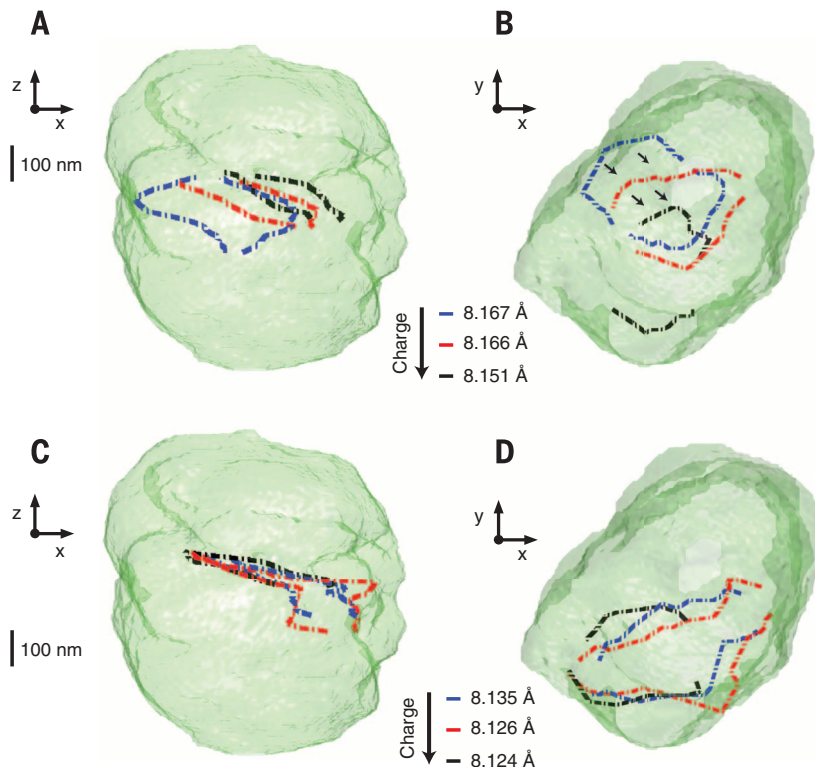


Fig. 3. Three-dimensional edge dislocation line evolution due to charging. The particle shape is represented by a semitransparent green isosurface. (A) Evolution of the dislocation line at three different charge states. (B) The same evolution as in (A) for a different view. (C) Evolution of the dislocation line for the subsequent three charge states. (D) The same evolution as in (C) for a different view.

and dynamic under applied current. There is inhomogeneity in the amount of movement among different line segments, and it does not appear to be random. Instead, there is preferential movement toward the boundary of the particle. Additional time sequences are shown in fig. S10.

We perform fits as shown in Fig. 2 to all dislocations as a function of charge state in order to locally determine the Poisson's ratio in the single particle along the dislocation line (27). Figure 4A shows Poisson's ratio of the particle in the vicinity of the dislocation line as a function of charge state. At full lithiation (discharged), the

local Poisson's ratio is in excellent agreement with the literature value of 0.3 (29). However, the lithium concentration changes as a function of voltage and is known to change material properties, including Young's modulus (30) and the diffusion coefficient (31). Surprisingly, we observe that Poisson's ratio decreases during delithiation, eventually becoming negative at roughly 4.5 V .

The negative Poisson's ratio, or auxetic property, could be due to the peculiar structural changes in LNMO. It is known that materials are auxetic for a variety of reasons, including the presence of microstructures, such as reentrant honeycombs,

and as a result of phase transformations (32). For example, auxetic behavior was attributed to a hinge-like structure in spinel CoFe_2O_4 (33), which has the same structure as LNMO. We hypothesize that a hinge-like mechanism as diagrammed in Fig. 4C is responsible for the reduction in the measured Poisson's ratio. At 4.5 V and higher, all of the Mn^{3+} ions are oxidized to Mn^{4+} , which

makes the Mn-O bond exceptionally strong because of the superior ligand field stabilization energy of Mn^{4+} due to its half-filled t_{2g} level (23). This leads to strong and weak bonds within the crystal, and ultimately to the hinge structure. As the voltage is increased and more lithium is removed, the hinge structure moves more freely and consequently the Poisson's ratio decreases.

If our hypothesis is correct, the delithiated LNMO spinel would be incredibly strain tolerant (34) and might be used to prevent structural collapse in layered oxide materials at high voltages when blended as a nanocomposite (35). The auxetic property may also explain why this material is relatively resistant to losing oxygen from the crystal structure at high voltage.

Near 4.7 V, LNMO exhibits two-phase coexistence and a structural phase transformation during charge and discharge, as evidenced by both electrochemical and diffraction data (24, 25, 36). The two phases differ in their lattice constant, whereas the symmetry group of the crystal remains the same. At the single-particle level, the phase transformation manifests itself as a splitting in the (111) diffraction peak, indicating that two lattice constants are present (see fig. S12 for diffraction data during the onset of the phase transformation and fig. S9 for single-particle lattice constant evolution). Figure S13 shows diffraction data midway through the phase transformation. Figure 5 shows the displacement and strain field evolution within the nanoparticle at two measurement times (left and right) corresponding to 4.7 and 4.69 V during the onset of the phase transformation during discharge. Again, the x axis corresponds to the [111] direction.

In Fig. 5A, we qualitatively identify an edge dislocation by inspection of the displacement field. Approximately 20 nm higher, the Li-rich phase nucleated above the dislocation and created tensile strain due to its larger lattice constant. However, this is below the spatial resolution of the experiment, and thus another cross-section (z_3) that is 40 nm higher is also shown to corroborate the previous statement. Thus, the observed dislocation is near the phase boundary between the Li-rich and Li-poor phase. From their proximity, we

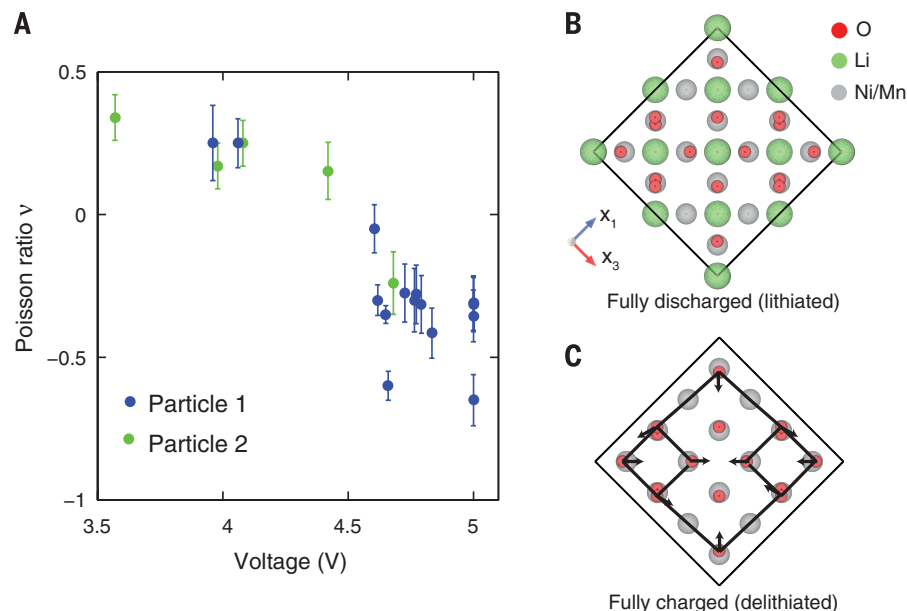


Fig. 4. The evolution of the local Poisson's ratio as a function of voltage and the proposed auxetic mechanism occurring in the LNMO unit cell. (A) Poisson's ratio values measured as a function of voltage for the particle discussed in the main text. Green points correspond to results from an additional measurement on a separate particle in another LNMO cathode battery (see fig. S11). (B and C) The LNMO unit cell when viewed along a primitive cubic lattice vector (x_1 and x_3 are the other primitive cubic lattice vectors) for the fully lithiated (discharged) and fully delithiated (charged) state, respectively. The proposed auxetic reentrant honeycomb structure is shown in black in (C).

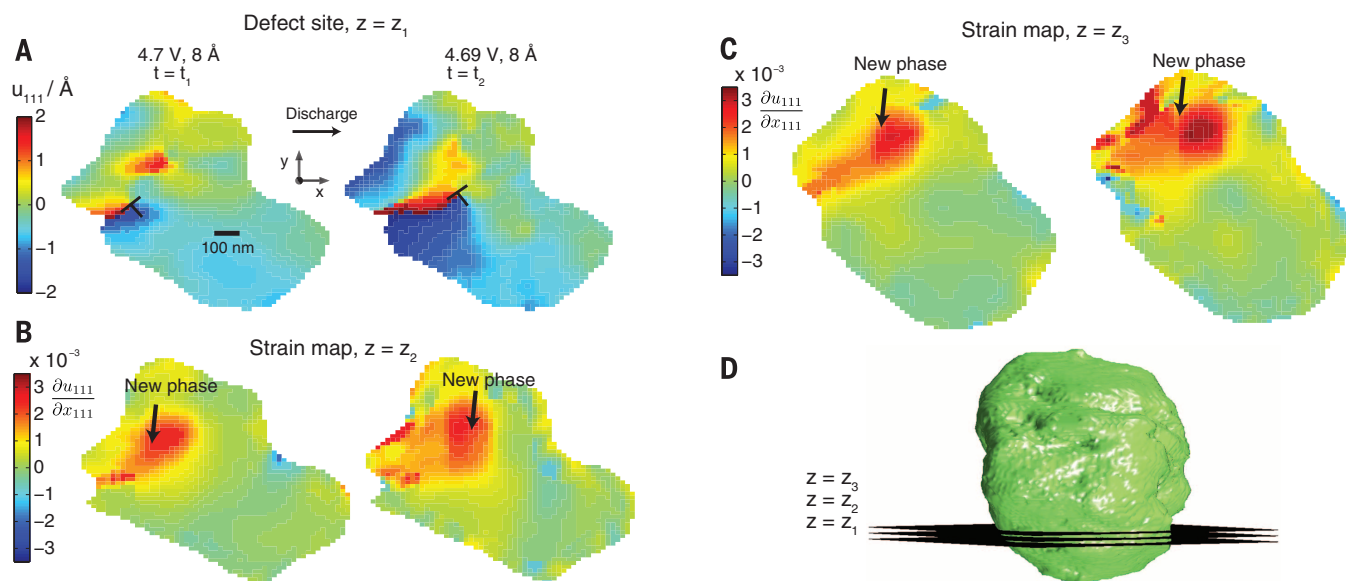


Fig. 5. Displacement and strain dynamics during the onset of the structural phase transformation. The displacement field within the particle is measured during the structural phase transformation during discharge. (A) The time evolution of a displacement field cross section with the edge dislocation indicated. (B) The time evolution of the compressive/tensile strain field in the [111] direction ($\partial_{111}u_{111}$) at one cross-section higher than in (A). The new phase manifests itself as tensile (positive) strain and is shown in red. (C) The strain field evolution at another, higher cross-section. (D) A green isosurface representing the particle shape. Black planes show the location of the cross-sections displayed in (A) to (C).

conclude that the dislocation likely acts as a nucleation point for the new phase during the phase transformation, which is expected from theoretical calculations (37). Figure 5, B and C, show that further discharge causes the Li-rich phase to expand further into the particle, as opposed to nucleating a new phase region a considerable spatial distance away. This suggests the near-equilibrium pathway for the phase transformation at the single-particle level. The observation of a phase boundary is quite interesting in light of recent results showing the absence of a phase boundary during fast charging in LiFePO_4 (38). The relatively slow cycling rate (4 hours for full charge) used in this study is most likely responsible for this discrepancy.

We studied topological defect dynamics in crystalline nanoparticles under operando conditions using Bragg coherent diffractive imaging. Edge dislocations that are static at room temperature are dynamic in response to charge transport. The 3D dislocation displacement field serves as a local probe of elastic properties, and we observe that at high voltage, Poisson's ratio in the vicinity of the dislocation is vastly different from that at lower voltages. This calls for further investigation into using lithium ions to tune material properties and could explain why LNMO is resistant to oxygen loss at high voltage. We anticipate that imaging of dislocations can be used as a nanotechnology to locally probe elastic properties in nanomaterials and that LNMO could improve the strain tolerance of other cathodes. We reconstructed the onset of the phase transformation, observed the dislocation act as a nucleation point, and showed how the phase expands into the particle. Our results open up the imaging of weakly strained phase transformations to BCDI and unlock the potential for a synthesis/imaging feedback loop to engineer dislocations at the nanoscale.

REFERENCES AND NOTES

- M. Fichtner, *Phys. Chem. Chem. Phys.* **13**, 21186–21195 (2011).
- N. Shin, M. Chi, J. Y. Howe, M. A. Filler, *Nano Lett.* **13**, 1928–1933 (2013).
- L. D. Carr, M. T. Lusk, *Nat. Nanotechnol.* **5**, 316–317 (2010).
- M. J. Hytch, J. L. Putaux, J. M. Pénisson, *Nature* **423**, 270–273 (2003).
- H. F. Poulsen, *Three-Dimensional X-ray Diffraction Microscopy* (Springer, Berlin, 2004).
- B. K. Tanner, *X-ray Diffraction Topography* (Pergamon, Oxford, 1976).
- G. N. Ramchandran, *Proc. Indiana Acad. Sci.* **19**, 280 (1945).
- J. B. Newkirk, *Phys. Rev.* **110**, 1465–1466 (1958).
- A. R. Lang, *J. Appl. Phys.* **29**, 597 (1958).
- A. R. Lang, A. P. W. Makepeace, *J. Phys. D Appl. Phys.* **32**, A97 (1999).
- D. Le Bolloch et al., *Phys. Rev. Lett.* **95**, 116401 (2005).
- P. Cloetens et al., *Proc. SPIE* **4503**, 82 (2002).
- Y. Takahashi et al., *Phys. Rev. B* **87**, 121201 (2013).
- B. Abbey, *JOM* **65**, 1183–1201 (2013).
- J. N. Clark et al., *Science* **341**, 56–59 (2013).
- G. J. Williams, M. A. Pfeifer, I. A. Vartanyants, I. K. Robinson, *Phys. Rev. Lett.* **90**, 175501 (2003).
- A. Ulvestad et al., *Nano Lett.* **14**, 5123–5127 (2014).
- A. Ulvestad et al., *Appl. Phys. Lett.* **104**, 073108 (2014).
- H. Wang, Y. Jang, B. Huang, *J. Electrochem. Soc.* **146**, 473 (1999).
- H.-Y. Shadow Huang, Y.-X. Wang, *J. Electrochem. Soc.* **159**, A815 (2012).
- A. Van der Ven, C. Marianetti, D. Morgan, G. Ceder, *Solid State Ion.* **135**, 21–32 (2000).
- J.-M. Tarascon, M. Armand, *Nature* **414**, 359–367 (2001).
- B. Xu, S. Meng, *J. Power Sources* **195**, 4971–4976 (2010).
- J.-H. Kim, S.-T. Myung, C. S. Yoon, S. G. Kang, Y.-K. Sun, *Chem. Mater.* **16**, 906–914 (2004).

- A. Singer et al., *Nano Lett.* **14**, 5295–5300 (2014).
- K. Saravanan, A. Jarry, R. Kostecki, G. Chen, *Sci. Rep.* **5**, 8027 (2015).
- Materials and methods are available as supplementary materials on Science Online.
- D. Hull, D. J. Bacon, *Introduction to Dislocations* (Butterworth-Heinemann, Oxford, ed. 5, 2011).
- J. Christensen, J. Newman, *J. Electrochem. Soc.* **153**, A1019 (2006).
- S. Lee, J. Park, A. M. Sastry, W. Lu, *J. Electrochem. Soc.* **160**, A968–A972 (2013).
- M. Yang et al., *Chem. Mater.* **23**, 2832–2841 (2011).
- G. N. Greaves, A. L. Greer, R. S. Lakes, T. Rouxel, *Nat. Mater.* **10**, 823–837 (2011).
- M. Valant, A.-K. Axelsson, F. Aguesse, N. M. Alford, *Adv. Funct. Mater.* **20**, 644–647 (2010).
- K. E. Evans, A. Alderson, *Adv. Mater.* **12**, 617–628 (2000).
- M. S. Whittingham, *Chem. Rev.* **104**, 4271–4302 (2004).
- R. A. Huggins, *Advanced Batteries: Materials Science Aspects* (Springer, New York, 2008).
- C. Collins, *Acta Metall.* **18**, 1209–1215 (1970).
- H. Liu et al., *Science* **344**, 1252817 (2014).

ACKNOWLEDGMENTS

This work was supported by the U.S. Department of Energy (DOE), Office of Science, Office of Basic Energy Sciences, under contract DE-SC0001805. H.M.C. and Y.S.M. acknowledge support on the

in situ CXDI cell design, materials synthesis, electrochemical and materials characterization from the NorthEast Center for Chemical Energy Storage (NECCES), an Energy Frontier Research Center funded by the U.S. Department of Energy, Office of Science, Basic Energy Sciences under Award no. DE-SC0012583. O.G.S. and Y.S.M. are grateful to the University of California–San Diego Chancellor's Interdisciplinary Collaborators Award that made this collaboration possible. J.N.C. gratefully acknowledges financial support from the Volkswagen Foundation. This research used resources of the Advanced Photon Source, a U.S. DOE Office of Science User Facility operated for the DOE Office of Science by Argonne National Laboratory under contract no. DE-AC02-06CH11357. We thank the staff at Argonne National Laboratory and the Advanced Photon Source for their support. The data are deposited at Sector 34-ID-C of the Advanced Photon Source.

SUPPLEMENTARY MATERIALS

www.sciencemag.org/content/348/6241/1344/suppl/DC1
Materials and Methods
Supplementary Text
Figs. S1 to S13
References (39–44)

21 October 2014; accepted 15 May 2015
10.1126/science.aaa1313

MEMBRANE FILTRATION

Sub-10 nm polyamide nanofilms with ultrafast solvent transport for molecular separation

Santanu Karan, Zhiwei Jiang, Andrew G. Livingston*

Membranes with unprecedented solvent permeance and high retention of dissolved solutes are needed to reduce the energy consumed by separations in organic liquids. We used controlled interfacial polymerization to form free-standing polyamide nanofilms less than 10 nanometers in thickness, and incorporated them as separating layers in composite membranes. Manipulation of nanofilm morphology by control of interfacial reaction conditions enabled the creation of smooth or crumpled textures; the nanofilms were sufficiently rigid that the crumpled textures could withstand pressurized filtration, resulting in increased permeable area. Composite membranes comprising crumpled nanofilms on alumina supports provided high retention of solutes, with acetonitrile permeances up to 112 liters per square meter per hour per bar. This is more than two orders of magnitude higher than permeances of commercially available membranes with equivalent solute retention.

Many separation processes used by industry require evaporation and distillation, which have high energy consumption due to the latent heat of vaporization. Membrane technology would require only one-tenth as much energy to process an equivalent amount of liquid (J), but for industrial processes involving large quantities of organic liquids, such membranes should be stable in organic solvents and have high permeance to enable processing within a reasonable time. Thin-film composite (TFC) membranes for water desalination (2, 3), which comprise a polyamide separating layer formed by interfacial polymerization on top of a porous ultrafiltration support

membrane, have been adapted for organic solvent nanofiltration (OSN). However, the permeance of TFC-OSN membranes is still relatively low (~ 2.5 liters m^{-2} hour^{-1} bar^{-1} for membranes that reject $>90\%$ of solutes with molecular weight <300 g mol^{-1}) (4), demanding large membrane areas for industrial applications. Meanwhile, for OSN, Karan et al. (5) used chemical vapor deposition to prepare diamond-like carbon (DLC) nanosheet membranes that showed ultrafast permeance when the thickness of the DLC separation layer was decreased to 30 nm; the DLC layer remained mechanically robust. In contrast, when the same thickness-reduction approach was followed for solution-cast films of a linear polymer (PIM-1), a maximum heptane permeance of ~ 18 liters m^{-2} hour^{-1} bar^{-1} was measured for a film 140 nm thick, after which permeance decreased with decreasing thickness. This was attributed

Department of Chemical Engineering, Imperial College London, South Kensington Campus, London SW7 2AZ, UK.
*Corresponding author. E-mail: a.livingston@imperial.ac.uk

This copy is for your personal, non-commercial use only.

If you wish to distribute this article to others, you can order high-quality copies for your colleagues, clients, or customers by [clicking here](#).

Permission to republish or repurpose articles or portions of articles can be obtained by following the guidelines [here](#).

The following resources related to this article are available online at www.sciencemag.org (this information is current as of June 18, 2015):

Updated information and services, including high-resolution figures, can be found in the online version of this article at:

<http://www.sciencemag.org/content/348/6241/1344.full.html>

Supporting Online Material can be found at:

<http://www.sciencemag.org/content/suppl/2015/06/17/348.6241.1344.DC1.html>

This article **cites 38 articles**, 8 of which can be accessed free:

<http://www.sciencemag.org/content/348/6241/1344.full.html#ref-list-1>

This article appears in the following **subject collections**:

Chemistry

<http://www.sciencemag.org/cgi/collection/chemistry>

Materials Science

http://www.sciencemag.org/cgi/collection/mat_sci